

Variation of focusing patterns of laterally migrating particles in a square-tube flow due to non-Newtonian elastic force

Naoto Yokoyama,¹ Hiroshi Yamashita,^{2,3} Kento Higashi,² Yuta Miki,² Tomoaki Itano,² and Masako Sugihara-Seki^{2,3}

¹*Department of Mechanical Engineering, Tokyo Denki University, Adachi 120-8551, Japan*

²*Department of Pure and Applied Physics, Kansai University, Suita 564-8680, Japan*

³*Department of Mechanical Science and Bioengineering, Osaka University, Toyonaka 560-8531, Japan*

(Dated: June 15, 2021)

The elasto-inertial effects on particle focusing in a square-tube flow were investigated experimentally and numerically. Microscale experiments using spherical particles in dilute polymer solutions demonstrated that the particles are focused on the midline and/or the diagonal in a downstream cross-section, depending on the polymer concentration. Numerical computations based on the FENE-P model for the viscoelastic flow reproduced these focusing patterns. It was revealed that the transitions among the patterns are accounted for by the elastic forces due to the first normal stress difference and the polymer elongation, which are the essentials of the viscoelastic fluid.

Lift due to inertia causes particles suspended in a tube flow to travel the streamwise direction and to migrate in the lateral direction perpendicular to the mainstream. This phenomenon is called the Segré–Silberberg (SS) effect [1]. Inertial particles in circular-tube flows appear only at the so-called SS annulus in the downstream cross-section at small Reynolds numbers Re . The radius of the SS annulus is roughly 0.6 times as large as the tube radius, and is determined by a balance between the lift due to the shear gradient and the wall effect [2]. On the other hand, in square-tube flows, which lack the axial symmetry, inertial particles appear at isolated focusing positions instead of the SS annulus located on the midline, diagonal, and others [3–5]. Various focusing patterns emerge, depending on Re and the blockage ratio $\kappa = d/W$, where d and W respectively represent the particle diameter and the tube width [4, 6–8]. For deformable particles such as living cells, their deformability also affects their focusing positions [9]. If the focusing positions can be controlled by the size, shape, and rheological properties such as the deformability of the suspended particles, the SS effect can be used for particle separation and sorting. To this end, extensive studies have been performed to apply the SS effect to a suspension flow of living cells and particles in microfluidics. The development of continuous and easy separation as well as the purification of living cells without damage is strongly required especially in life science and medical care including clinical practice [10].

The medium where living cells are suspended usually contains polymers such as proteins and has viscoelasticity. In a viscoelastic tube flow, suspended particles experience the lift due to elasticity, which points inwards except near the corner in the cross-section [11]. Even in an almost Newtonian fluid medium with a short relaxation time, the large shear strain can cause a notable non-Newtonian behavior [12]. Moreover, the controllability of the focusing characteristics by the rheological properties of the medium has also been reported [13].

Most previous studies on the particle migration in viscoelastic flows concern the particle focusing on the tube center and the tube corner [14–16]. However, as flow rates increase to realize a high throughput, inertial effects on the particle migration are enhanced as Re increases. Since the inertial lift due to the shear gradient directs outwards as opposed to inward lift due to elasticity, the particle focusing position should vary owing to the interplay between inertia and elasticity. In fact, a recent numerical study based on the Oldroyd-B model predicted that suspended spherical particles in square-tube flows focus on the midline and diagonal as well as at the tube center and tube corners, depending on the Weissenberg number Wi [17]. On the other hand, few experimental observations have reported the focusing of particles at the intermediate positions between the tube center and the tube wall. Thus, the combined effects of the inertia and elasticity of the media on the focusing remain unclear yet.

Here, we experimentally investigate the migration of spherical particles suspended in square-tube flows of dilute polymer (polyvinylpyrrolidone, PVP) solutions to demonstrate the presence of intermediate focusing positions of particles. To explain the focusing patterns in the viscoelastic flow, we also performed numerical computations for a neutrally buoyant spherical particle in viscoelastic fluids flowing through a square tube based on the finitely extensible nonlinear elastic-Peterlin (FENE-P) model [18]. The lateral force due to the elasticity acting on the particle is quantitatively evaluated, and the transition of the focusing pattern is rationalized in terms of the first normal stress difference and the polymer elongation near the tube wall.

In the laboratory experiment, spherical polystyrene particles dilutely suspended in aqueous solutions of PVP, biocompatible synthetic polymers, flowing through a square tube were observed to detect their positions in a cross-section. Figure 1(a) shows the experimental system (see Ref. [4] for details). The solutions contain PVP ($M_w = 360\text{kDa}$, Tokyo Chemical Industry) at the concentrations of $\phi = 1, 1.9, \text{ and } 2.5 \text{ wt\%}$, whose viscosities are $\eta = 3.2, 7.4, \text{ and } 10 \text{ mPa}\cdot\text{s}$ at $22 \text{ }^\circ\text{C}$, respectively. These viscosity values were measured using a rotational rheometer (Haake Mars III) and are nearly independent of the shear rate. Their elasticities are too small to evaluate the relaxation time

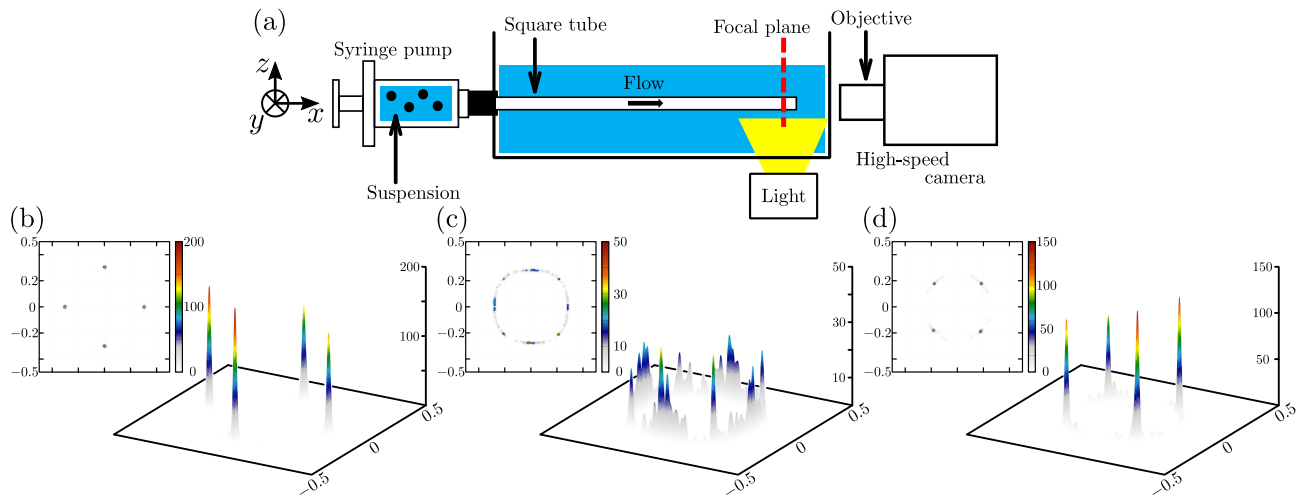


FIG. 1. Focusing positions in the PVP-solution experiments. (a) Experimental setup (schematic). (b)–(d) Existence probability of particles on a cross-section near the outlet of the tube with the PVP concentrations (b) $\phi = 1$ wt%, (c) $\phi = 1.9$ wt%, and (d) $\phi = 2.5$ wt%. ($Re = 50$ and $\kappa = 0.15$)

from the dynamic moduli, and hence Wi in these experiments could not be evaluated. Since the PVP solution is dilute, the non-Newtonian properties are quite weak. Spherical polystyrene particles (diameter $d = 60 \mu\text{m}$) were suspended in the PVP solution with volume fractions of order 10^{-2} %. A syringe pump (Nexus 6000, ISIS) was used to infuse the suspension through a straight glass duct (VitroCom) with a square cross-section of the width $W = 400 \mu\text{m}$ and a length $L = 600$ mm. The syringe and the duct were connected via a circular tube with inner diameter of 1.14 mm, and the contraction ratio is approximately 1/3. Moreover, the Poiseuille flow is built roughly at $x/W \approx Re/30 \approx 1.7$ and the entrance effects are negligible. More than 500 particles were imaged in the cross-section near the outlet of the tube with a high-speed camera (AX100, Photron) equipped with $20\times$ objective, and the particle positions were determined by image analysis (Image J [19], NIH). The Reynolds number was set to be $Re = UW/\nu = 50$, which results in the particle Reynolds number $Re_p = Re \kappa^2 = 1.125$. The blockage ratio is $\kappa = 0.15$. Here, U and ν are the mean velocity and the kinematic viscosity, respectively. The x -axis corresponds to the centerline of the tube, and the y - and z -axes, which are normal to the tube walls, span the cross-section. In addition to the Cartesian coordinate (y, z) , the polar coordinate (r, θ) is also used in the cross-section.

Figures 1(b)–(d) show the existence probability of particles on a cross section near the outlet of the tube for various PVP concentrations. In the most dilute PVP solution ($\phi = 1$ wt%, Fig. 1(b)), the particles are focused on the midlines of the cross-section similar to Newtonian flows [4, 7]. These focusing positions are referred to as the midline equilibrium position (MEP). As the PVP concentration increases, new focusing positions, which are referred to as the diagonal equilibrium positions (DEP), emerge on the diagonal for $\phi = 1.9$ wt% (Fig. 1(c)). For $\phi = 1.9$ wt%, the MEP and the DEP are bistable, and the particles are focused near these eight equilibrium positions. Some particles do not reach the focusing positions completely yet, and the ratio $L/W = 1500$ might not be large enough for $\phi = 1.9$ wt%. [20] However, because the existence probabilities of the particles at the focusing positions are much larger than those out of the focusing positions, the focusing positions from these experiments are clearly identified. Further increasing the PVP concentration eliminates the MEP, and the particles are focused only near the DEP for $\phi = 2.5$ wt% (Fig. 1(d)). Figures 1(b)–(d) demonstrate that the three focusing patterns and the transitions among them emerge for $Re = 50$ and $\kappa = 0.15$ as the PVP concentration increases. It is noteworthy that particle focusing on the tube center is also observed in higher-concentration PVP solutions ($\phi = 8$ wt%) at low Re . This is consistent with the previous study [15], but the result is not shown here.

The Weissenberg number Wi is defined as the ratio of the elastic force to the viscous force and is considered to increase as the PVP concentration increases. Numerical computations by using the FENE-P model for the viscoelastic flow were performed to find the lift distribution and the focusing positions, which are sinks of the vector field of the lift, depending on Wi in comparison with the above experiment.

The governing equation nondimensionalized by the mean-flow velocity and the tube width is written as

$$\frac{\partial \mathbf{u}}{\partial t} + (\mathbf{u} \cdot \nabla) \mathbf{u} = -\nabla p + \frac{\beta}{Re} \nabla^2 \mathbf{u} + \nabla \cdot \boldsymbol{\tau}_p + \mathbf{f}_{IB} + \mathbf{f}_{PG}, \quad (1)$$

$$\nabla \cdot \mathbf{u} = 0, \quad (2)$$

where \mathbf{u} , p , and τ_p are respectively the velocity of the flow, the pressure, and the viscoelastic stress tensor derived from the polymers. Moreover, $1/\text{Re}$ is the nondimensionalized total shear viscosity. The ratio of the shear viscosity due to the solvent Newtonian fluid to the total viscosity is expressed by β , and $\beta = 1/2$ in this Letter. Note that the non-dimensional lateral velocity is smaller than 10^{-6} in the absence of the particle at $\text{Re} = 50$ in the Wi range examined in this Letter, and the secondary flow is negligible, since the non-Newtonian properties are weak. The interaction between the inertial particles and the flow is modeled by the volume force \mathbf{f}_{IB} according to the immersed boundary method [21]. The flow is driven by the mean pressure gradient \mathbf{f}_{PG} , so that the volume flux is constant. To compare the focusing positions in the experiments and the numerical computations, $\text{Re} = 50$ and $\kappa = 0.15$ are employed.

The viscoelastic fluid of the dilute polymer solutions is modeled by the FENE-P model, where the viscoelastic stress tensor τ_p is given by the positive-definite symmetric conformation tensor \mathbf{C} :

$$\tau_p = \frac{1-\beta}{\text{ReWi}} \left(\frac{\mathbf{C}}{1 - \text{tr}(\mathbf{C})/l^2} - \mathbf{I} \right). \quad (3)$$

Here, the maximal length of the polymers l is set to 10. The square-root symmetric tensor \mathbf{B} instead of $\mathbf{C} = \mathbf{B}^2$ is employed for numerical stability [22], and the governing equation of \mathbf{B} is written as

$$\frac{\partial \mathbf{B}}{\partial t} = -\mathbf{u} \nabla \mathbf{B} + \mathbf{B} \nabla \mathbf{u} + \mathbf{A} \mathbf{B} + \frac{1}{2\text{Wi}} \left(\mathbf{B}^{-1} - \frac{\mathbf{B}}{1 - \text{tr}(\mathbf{B}^2)/l^2} \right), \quad (4)$$

where \mathbf{A} is the antisymmetric tensor that satisfies $\mathbf{A} \mathbf{B} + \mathbf{B} \mathbf{A} = (\nabla \mathbf{u})^T \mathbf{B} - \mathbf{B} \nabla \mathbf{u}$.

These governing equations are numerically integrated by a fractional-step method. The Adams–Bashforth method is used for the convection term and the non-Newtonian viscous term in the Navier–Stokes equation (1), and the Newtonian viscous term is implicitly added. The mean pressure gradient is determined by the parameter adaptive control so that the mean velocity is unity. The Poisson equation for the pressure is solved by the biconjugate gradient stabilized (BiCGStab) method or the successive over relaxation (SOR) method. The Adams–Bashforth method is used also for the governing equation of \mathbf{B} (4) and that of the particle motion (7) below. The periodic boundary condition is used in the streamwise direction with a period length $L_x = 2$. That is, the period length is twice as long as the tube width, and more than 13 times longer than the particle’s diameter. The relative difference of the lateral force acting on the particle placed at $(y_C, z_C) \approx (0.174, 0)$ at $\text{Wi} = 0.16$ between $L_x = 1$ and $L_x = 4$ is approximately 3%, and that between $L_x = 2$ and $L_x = 4$ is approximately 1%. These small relative differences validate the period length $L_x = 2$ as well as the periodic boundary condition.

The volume force by using the immersed boundary method is given as

$$\mathbf{f}_{\text{IB}} = \frac{\alpha}{\Delta t} (\mathbf{U} - \mathbf{u}^*), \quad (5)$$

where \mathbf{U} and \mathbf{u}^* are respectively the particle’s rigid-body velocity at the center of each computational cell near the particle and the intermediate velocity of the flow [21]. Here, α represents the volume fraction of the inertial particles in the computational cell. The force and the torque acting on the particle are respectively the reaction force and torque of the volume force, and obtained as

$$\mathbf{F}_{3\text{D}} = \int (-\mathbf{f}_{\text{IB}}) dV, \quad \mathbf{N} = \int (\mathbf{x} - \mathbf{x}_C) \times (-\mathbf{f}_{\text{IB}}) dV. \quad (6)$$

The projection of the three-dimensional force $\mathbf{F}_{3\text{D}}$ onto the cross-section, that is, the lift acting on the particle \mathbf{F} is investigated in this Letter. The particles are fixed in the lateral direction while they travel in the streamwise direction and rotate freely. Thus, the equation of motion for the streamwise velocity U_{C_x} of the center of mass of the particle \mathbf{x}_C and the angular velocity $\boldsymbol{\Omega}_C$ is written as

$$m \frac{dU_{C_x}}{dt} = F_{3\text{D}x}, \quad I \frac{d\boldsymbol{\Omega}_C}{dt} = \mathbf{N}. \quad (7)$$

The mass and the inertial moment of the particles are expressed by $m = \pi\kappa^3/6$ and $I = m\kappa^2/10$, respectively.

Figures 2(a)–(b) plot the radial component of lift F_r acting on the particle placed on the midline (y -axis) and the diagonal. Note that $F_r = F_y$ on the y -axis. The lift in Newtonian flows is directed outward, i.e., $F_r > 0$ near the tube center while $F_r < 0$ near the tube wall [7, 23]. As Wi increases, F_r decreases except on the diagonal near the tube wall, i.e., tube corners ($r \gtrsim 0.5$ in Fig. 2(b)), and the zeros of F_r slightly move closer to the origin in the range $0 \leq \text{Wi} \leq 0.25$. Note that these zeros correspond to the MEP (Fig. 2(a)) and the DEP (Fig. 2(b)) because $F_\theta = 0$ on

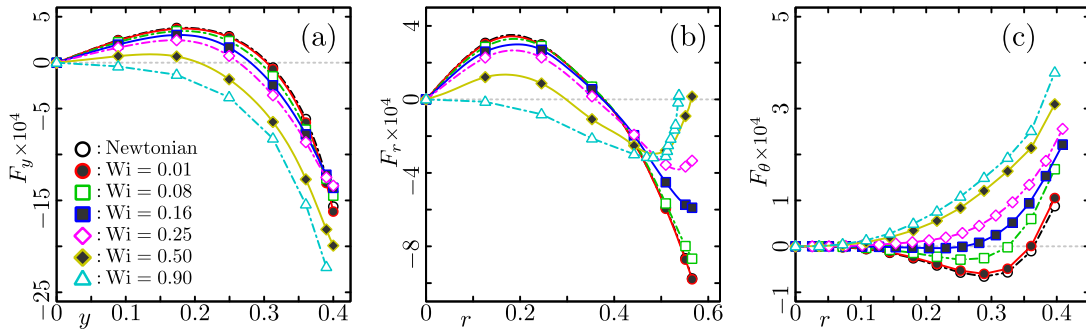


FIG. 2. Radial component of the lift exerted on the particle located (a) on the midline and (b) on the diagonal. Azimuthal component of the lift exerted on the particle located (c) on the line $z = y \tan(\pi/8)$.

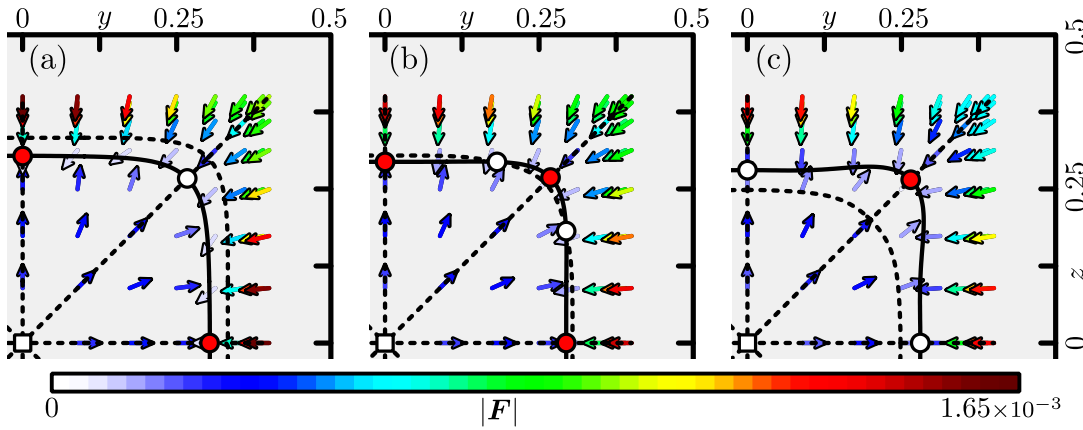


FIG. 3. Lift and equilibrium positions. Stable, saddle, and unstable equilibrium positions are respectively represented by \bullet , \circ , and \square . The solid line and the dashed lines represent the contour of $F_r = 0$, and those of $F_\theta = 0$, respectively. Each arrow represents the lift direction with its magnitude shown by color. (a) $Wi = 0.01$, (b) $Wi = 0.08$, and (c) $Wi = 0.16$.

these lines. These zeros of F_r disappear because $F_r < 0$ except near the corners for the large $Wi (= 0.9)$. This result implies that the inward lift acts on the particle at large Wi similar to previous studies [15, 17].

For a large $Wi (= 0.9)$, $F_r < 0$ at $r \lesssim 0.52$ while $F_r > 0$ at $r \gtrsim 0.52$ on the diagonal (Fig. 2(b)). Thus, the tube center becomes a stable equilibrium position, and another focusing position appears near the corner outside of the saddle position where the particle almost touches the two walls. Therefore, the corner equilibrium positions as well as the center are predicted to be focusing positions for $Wi \gtrsim 0.9$.

Similarly, Fig. 2(c) plots the azimuthal component of lift F_θ acting on the particle placed on a line of $z = y \tan(\pi/8)$. The azimuthal lift F_θ increases monotonically and the zeros of F_θ approach the origin with increasing Wi . At the large $Wi (= 0.9)$ these zeros vanish with $F_\theta > 0$ on a line of $z = y \tan(\pi/8)$. This result indicates that the lift acts towards the diagonal at large Wi , because the sign of F_θ in $\pi/4 < \theta < \pi/2$ is opposite to that in $0 < \theta < \pi/4$ from the symmetry. As shown in Fig. 4 below, the lift toward the diagonal is one of the most important features of the elastic lift.

Figure 3 shows the lift in the first quadrant of the cross-section for $Wi = 0.01, 0.08$, and 0.16 . Stable, saddle, and unstable equilibrium positions are also displayed, and the focusing positions observed experimentally correspond to the stable equilibrium positions.

For the smallest $Wi (= 0.01)$, the lift in Fig. 3(a) is quite similar to that obtained in Newtonian flows [6, 7, 23]. The contour of $F_r = 0$ (r -nullcline) forms a closed loop almost parallel to the walls between the tube center and the tube walls. On the other hand, the contours of $F_\theta = 0$ consist of the midlines (y - and z -axes), the diagonal, and a closed loop just outside of the r -nullcline. Although all the contours of $F_\theta = 0$ are nullclines, here we refer only to the closed loop as θ -nullcline for convenience. Note that $F_r > 0$ inside the r -nullcline whereas $F_r < 0$ outside it. Similarly, $F_\theta < 0$ inside the θ -nullcline whereas $F_\theta > 0$ outside it in $0 < \theta < \pi/4$, and vice versa in $\pi/4 < \theta < \pi/2$.

From the symmetry, the tube center is always an equilibrium position, where the lift vanishes. The lift direction around the tube center indicates that the tube center is an unstable equilibrium position for $Wi = 0.01$. The intersections between the zero contours of F_r and F_θ represent the equilibrium position; the intersection between the

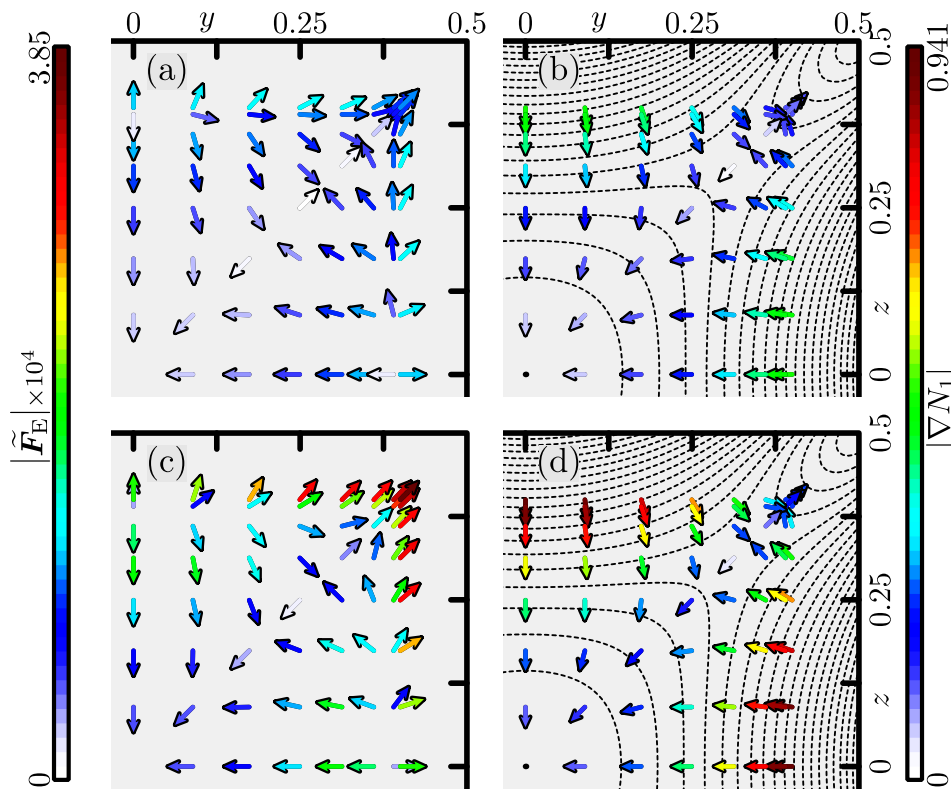


FIG. 4. (a) and (c): Alternative elastic lift $\tilde{\mathbf{F}}_E = \mathbf{F}_{W_i} - \mathbf{F}_0$. (b) and (d): Contours of N_1 for every 6.85×10^{-3} (b) and 1.31×10^{-2} (d). The arrows represent $-\nabla N_1$. (a)–(b) $Wi = 0.08$, and (c)–(d) $Wi = 0.16$.

r -nullcline and the midline (y - and z -axes) correspond to the MEP, and that between the r -nullcline and the diagonal does to the DEP. At $Wi = 0.01$, the MEP is stable, but the DEP is a saddle, judged from the lift direction around them. This predicts that the particle focuses on the MEP at small Wi , which agrees with the experiment of $\phi = 1$ wt% in Fig. 1(b).

At $Wi = 0.08$ in Fig. 3(b), the θ -nullcline approaches the tube center, whereas the r -nullcline does not change its position so much. Thus, these two nullclines cross, and the intersection represents another equilibrium position. The lift indicates that this new equilibrium position is a saddle, and both MEP and DEP are stable. This result is consistent with the experiment of $\phi = 1.9$ wt% in Fig. 1(c).

A further increase in Wi moves the θ -nullcline closer to the tube center. At $Wi = 0.16$, the θ -nullcline exists inside the r -nullcline (Fig. 3(c)). In this case, the MEP is unstable while the DEP is stable in accordance with the experiment of $\phi = 2.5$ wt% in Fig. 1(d).

The numerical results for $Wi \leq 0.16$ in Figs. 3(a)–(c) reproduce the focusing patterns obtained experimentally for $\phi \leq 2.5$ wt% (Figs. 1(b)–(d)). In the numerical computations, these patterns transition as Wi increases, which is proportional to the relaxation time λ of the medium. Although λ of the polymer solutions used in the experiments is currently difficult to measure, λ is reasonably assumed to increase with increasing ϕ . Thus, the present numerical computations explain both the focusing patterns and the transition among them shown in Fig. 1.

Figure 3 demonstrates that the transition of the particle focusing patterns is due to the immobility of the r -nullclines and the shrinkage of the θ -nullclines with increasing Wi (≤ 0.16). The focusing pattern is also consistent with that in an Oldroyd-B fluid flow [17]. These movements of the nullclines can be understood from an increase in lift due to elasticity \mathbf{F}_E , which would be directed inward and toward the diagonal. However, direct calculation of \mathbf{F}_E is difficult. Instead, \mathbf{F}_E is approximated by $\tilde{\mathbf{F}}_E = \mathbf{F}_{W_i} - \mathbf{F}_0$, where \mathbf{F}_{W_i} and \mathbf{F}_0 are the lifts acting on the particle placed at the same position in a finite- Wi flow and in a Newtonian flow ($Wi = 0$), respectively. We also computed the first normal stress difference N_1 using the flow in the absence of the particle, whose velocity profile is close to the Poiseuille flow. The variation of N_1 over the particle's diameter produces the lift $\mathbf{F}_{EN_1} = C_{N_1} \kappa^3 \nabla N_1$ in the present nondimensionalization, where the coefficient C_{N_1} is negative [11, 13–15].

In fact, $\tilde{\mathbf{F}}_E$ and $-\nabla N_1$ for $Wi = 0.08$ and 0.16 are qualitatively similar, and are mainly directed inward and toward the diagonal in the region far from the tube wall as illustrated in Fig. 4. Only near the tube wall, where the wall

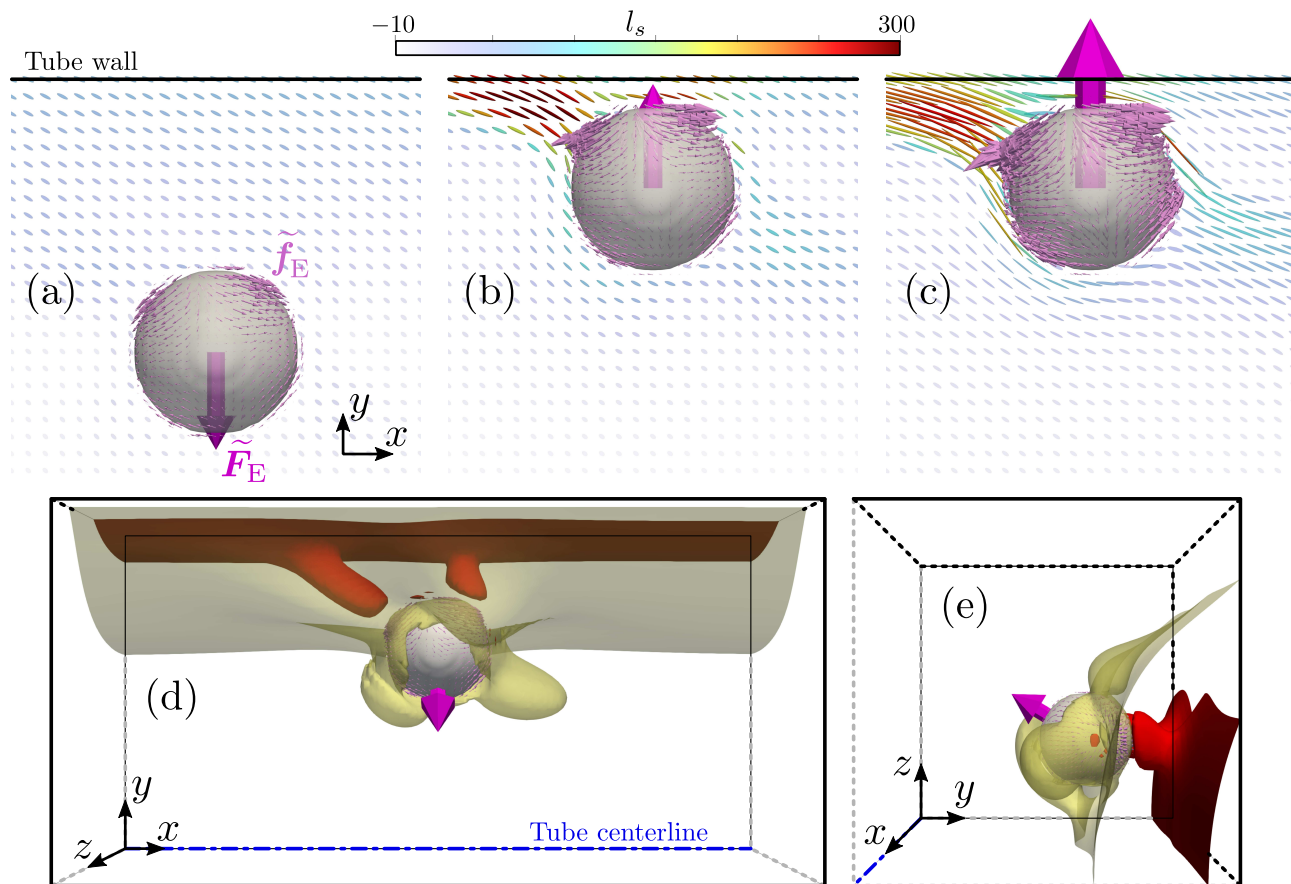


FIG. 5. (a)–(c) Conformation tensor on the z plane and the elastic force acting on the particle placed at (a) $(y_C, z_C) \approx (0.25, 0)$, and (b)–(c) $(y_C, z_C) \approx (0.4, 0)$. The ellipsoids colored by l_s represent the eigenvectors and eigenvalues of \mathbf{C} . (d)–(e) Isosurfaces of $l_s = 15$ (yellow) and 55 (red) and the elastic force when the particle center is approximately at $(y_C, z_C) \approx (0.31, 0.17)$. $Wi = 0.08$ except (e) $Wi = 0.16$.

effect due to the elasticity is significant, $\tilde{\mathbf{F}}_E$ is directed outward and toward the diagonal. Thus, the wall-induced elastic lift \mathbf{F}_{EW} is considered to be directed outward. Near the r -nullcline, i.e., the contour $F_r = 0$ in Fig. 3, $\tilde{\mathbf{F}}_E$ is directed toward the azimuthal direction, and hence the radial component of $\tilde{\mathbf{F}}_E$ nearly vanishes as seen in Figs. 4(a) and (c). This suggests that the radial components of \mathbf{F}_{EN_1} and \mathbf{F}_{EW} balance near the r -nullcline at small Wi . Since the magnitude of \mathbf{F}_{EN_1} is linearly proportional to Wi and that of \mathbf{F}_{EW} increases with Wi , the radial component of $\tilde{\mathbf{F}}_E$ ($\approx \mathbf{F}_{EN_1} + \mathbf{F}_{EW}$) remains approximately 0 near the r -nullcline independently of Wi . In contrast, the azimuthal component of $\tilde{\mathbf{F}}_E$ is directed toward the diagonal, and its magnitude increase with Wi there. Consequently, the θ -nullcline shrinks faster while the r -nullcline does not change its position, as Wi increases.

Next, we consider $\tilde{\mathbf{F}}_E$ in more detail based on the polymer stretch. While the mean-field behavior of the conformation tensor \mathbf{C} determines \mathbf{F}_{EN_1} , the interaction between \mathbf{C} near the wall and the particle's motion provides \mathbf{F}_{EW} . Figures 5(a)–(c) show the distribution of the elastic force acting on the particle $\tilde{\mathbf{f}}_E$, which is the difference of the interaction forces \mathbf{f}_{IB} between in a finite- Wi flow and in a Newtonian flow, and $\tilde{\mathbf{F}}_E$. The major and minor axes of the ellipsoids represent the eigenvectors and eigenvalues of \mathbf{C} , and the colors of the ellipsoids express the normalized polymer stretch defined as $l_s = (\text{tr}\mathbf{C} - 3)/(2Wi^2)$ [24].

Since the velocity profile is close to the Poiseuille flow, the large velocity gradient near the tube wall elongates the polymers. The difference of l_s between near the wall and near the tube center provides $-\nabla N_1$. This is consistent with the observation of $\tilde{\mathbf{f}}_E$ and $\tilde{\mathbf{F}}_E$ for the particle relatively far from the wall ($(y_C, z_C) \approx (0.25, 0)$, Fig. 5(a)); the inward force on the outside surface $y > y_C$ is larger than the outward force on the inside surface $y < y_C$, and the resultant $\tilde{\mathbf{F}}_E$ is directed inward. The small polymer deformation due to the interactions between the particle and the flow results in $\tilde{\mathbf{F}}_E \approx \mathbf{F}_{EN_1}$.

When the particle is located near the wall ($(y_C, z_C) \approx (0.4, 0)$, Fig. 5(b)), the strong elongation near the wall extends

to the particle from the upstream, which would generate \mathbf{F}_{EW} . The polymers elongated in the direction normal to the particle touch the particle on its upstream and outer side. The strongly elongated polymers generate tension, pulling the particle to the upstream and outward to the wall. Therefore, the inward force of $\tilde{\mathbf{f}}_E$ on the outer side for the particle near the wall is smaller than that for the particle far from the wall, which results in \mathbf{F}_{EW} directed outward. The outward \mathbf{F}_{EW} is larger than the inward \mathbf{F}_{EN_1} near the wall, and $\tilde{\mathbf{F}}_E \approx \mathbf{F}_{EW}$ is directed outward there. This behavior of $\tilde{\mathbf{F}}_E$ is enhanced as Wi increases (Fig. 5(c)).

When the particle is placed near the wall off the midline ($(y_C, z_C) \approx (0.31, 0.17)$), strongly elongated polymers appear in the upstream region with $y > y_C$ and $z > z_C$, and they provide \mathbf{F}_{EW} directed outward (Figs. 5(d)–(e)). On the other hand, $-\nabla N_1$ and hence \mathbf{F}_{EN_1} are directed inward and toward the diagonal. The radial components of \mathbf{F}_{EW} and \mathbf{F}_{EN_1} almost balance, and $\tilde{\mathbf{F}}_E \approx \mathbf{F}_{EW} + \mathbf{F}_{EN_1}$ is directed to the diagonal.

In this Letter, the focusing positions of spherical particles suspended in dilute PVP solutions observed in the laboratory experiment are reproduced by numerical computations based on the FENE-P model for the viscoelastic flow. In the laboratory experiment with $Re = 50$ and $\kappa = 0.15$, the four focusing positions appear each on the midlines and the diagonals when $\phi = 1$ wt% and 2.5 wt%, respectively. At $\phi = 1.9$ wt% between these two concentrations, the particles focus near these eight equilibrium positions, indicating that the MEP and the DEP are bistable. The focusing positions appear as sinks of the vector field of the lift in the numerical computations, and the transition of the focusing patterns due to the PVP concentration was replicated by changing Wi in the numerical computations. The elastic lift stems mainly from the inward lift due to the first normal stress difference and the outward lift due to the polymer elongation near the tube wall. The radial balance between these two major elements of the elastic lift makes the position of the contour of $F_r = 0$ independent of Wi . In contrast, the closed-loop contour of $F_\theta = 0$ shrinks, since these two elements are stronger and the elastic lift is directed more toward the diagonal as Wi increases. The position switch of the zero contours makes the MEP unstable and the DEP stable. This transition results from the interaction between the non-Newtonian properties of the PVP solution and the particle's motion. The lateral migration of particles reported in this Letter does not originate from the secondary flow, since the secondary flow is extremely weak due to the weak non-Newtonian properties of the medium.

ACKNOWLEDGMENTS

We thank Dr. Takeshi Matsumoto for his valuable advice on numerical computations based on the FENE-P model. We acknowledge Katsuhiko Uno for his support on the numerical computations. The numerical computations in this work were carried out at Research Institute for Information Technology, Kyushu University. This work was partially supported by KAKENHI Grant No. 20H02072 and No. 20H04504.

-
- [1] G. Segré and A. Silberberg, Behaviour of macroscopic rigid spheres in Poiseuille flow part 2. experimental results and interpretation, *J. Fluid Mech.* **14**, 136 (1962).
 - [2] J. P. Matas, J. F. Morris, and E. Guazzelli, Lateral forces on a sphere, *Oil Gas Sci. Tech. Rev. IFP* **59**, 59 (2004); B. P. Ho and L. G. Leal, Migration of rigid spheres in a two-dimensional unidirectional shear flow of a second-order fluid, *J. Fluid Mech.* **76**, 783 (1976).
 - [3] M. Abbas, P. Magaud, Y. Gao, and S. Geoffroy, Migration of finite sized particles in a laminar square channel flow from low to high Reynolds numbers, *Phys. Fluids* **26**, 123301 (2014).
 - [4] H. Shichi, H. Yamashita, J. Seki, T. Itano, and M. Sugihara-Seki, Inertial migration regimes of spherical particles suspended in square tube flows, *Phys. Rev. Fluids* **2**, 044201 (2017).
 - [5] B. Chun and A. J. C. Ladd, Inertial migration of neutrally buoyant particles in a square duct: An investigation of multiple equilibrium positions, *Phys. Fluids* **18**, 031704 (2006); K. Miura, T. Itano, and M. Sugihara-Seki, Inertial migration of neutrally buoyant spheres in a pressure-driven flow through square channels, *J. Fluid Mech.* **749**, 320 (2014); D. Di Carlo, D. Irimia, R. G. Tompkins, and M. Toner, Continuous inertial focusing, ordering, and separation of particles in microchannels, *Proc. Natl. Acad. Sci. USA* **104**, 18892 (2007); Y.-S. Choi, K.-W. Seo, and S.-J. Lee, Lateral and cross-lateral focusing of spherical particles in a square microchannel, *Lab Chip* **11**, 460 (2011).
 - [6] H. Yamashita, T. Itano, and M. Sugihara-Seki, Bifurcation phenomena on the inertial focusing of a neutrally buoyant spherical particle suspended in square duct flows, *Phys. Rev. Fluids* **4**, 124307 (2019).
 - [7] D. Di Carlo, J. F. Edd, K. J. Humphry, H. A. Stone, and M. Toner, Particle segregation and dynamics in confined flows, *Phys. Rev. Lett.* **102**, 094503 (2009).
 - [8] C. Prohm and H. Stark, Feedback control of inertial microfluidics using axial control forces, *Lab Chip* **14**, 2115 (2014).
 - [9] S. C. Hur, N. K. Henderson-MacLennan, E. R. B. McCabe, and D. Di Carlo, Deformability-based cell classification and enrichment using inertial microfluidics, *Lab Chip* **11**, 912 (2011); A. Kilimnik, W. Mao, and A. Alexeev, Inertial migration of deformable capsules in channel flow, *Phys. Fluids* **23**, 123302 (2011).

- [10] J. A. Davis, D. W. Inglis, K. J. Morton, D. A. Lawrence, L. R. Huang, S. Y. Chou, J. C. Sturm, and R. H. Austin, Deterministic hydrodynamics: Taking blood apart, *Proc. Natl. Acad. Sci. USA* **103**, 14779 (2006).
- [11] X. Lu, C. Liu, G. Hu, and X. Xuan, Particle manipulations in non-Newtonian microfluidics: A review, *J. Colloid Interface Sci.* **500**, 182 (2017).
- [12] B. Kim, S. S. Lee, T. H. Yoo, S. Kim, S. Y. Kim, S.-H. Choi, and J. M. Kim, Normal stress difference-driven particle focusing in nanoparticle colloidal dispersion, *Sci. Adv.* **5** (2019).
- [13] A. M. Leshansky, A. Bransky, N. Korin, and U. Dinnar, Tunable nonlinear viscoelastic “focusing” in a microfluidic device, *Phys. Rev. Lett.* **98**, 234501 (2007).
- [14] G. Li, G. H. McKinley, and A. M. Ardekani, Dynamics of particle migration in channel flow of viscoelastic fluids, *J. Fluid Mech.* **785**, 486 (2015).
- [15] K. W. Seo, Y. J. Kang, and S. J. Lee, Lateral migration and focusing of microspheres in a microchannel flow of viscoelastic fluids, *Phys. Fluids* **26**, 063301 (2014).
- [16] S. Yang, J. Y. Kim, S. J. Lee, S. S. Lee, and J. M. Kim, Sheathless elasto-inertial particle focusing and continuous separation in a straight rectangular microchannel, *Lab Chip* **11**, 266 (2011); J. Nam, H. Lim, D. Kim, H. Jung, and S. Shin, Continuous separation of microparticles in a microfluidic channel via the elasto-inertial effect of non-newtonian fluid, *ibid.* **12**, 1347 (2012); G. D’Avino, G. Romeo, M. M. Villone, F. Greco, P. A. Netti, and P. L. Maffettone, Single line particle focusing induced by viscoelasticity of the suspending liquid: theory, experiments and simulations to design a micropipe flow-focuser, *ibid.* **12**, 1638 (2012); F. Del Giudice, G. D’Avino, F. Greco, P. A. Netti, and P. L. Maffettone, Effect of fluid rheology on particle migration in a square-shaped microchannel, *Microfluid Nanofluidics* **19**, 95 (2015).
- [17] Z. Yu, P. Wang, J. Lin, and H. H. Hu, Equilibrium positions of the elasto-inertial particle migration in rectangular channel flow of Oldroyd-B viscoelastic fluids, *J. Fluid Mech.* **868**, 316 (2019).
- [18] A. Peterlin, Hydrodynamics of macromolecules in a velocity field with longitudinal gradient, *J. Polym. Sci. B Polym. Lett.* **4**, 287 (1966); R. B. Bird, P. J. Dotson, and N. L. Johnson, Polymer solution rheology based on a finitely extensible bead-spring chain model, *J. Nonnewton. Fluid Mech.* **7**, 213 (1980).
- [19] C. A. Schneider, W. S. Rasband, and K. W. Eliceiri, NIH image to ImageJ: 25 years of image analysis, *Nat. Methods* **9**, 671 (2012).
- [20] The numerical computation below evaluates the streamwise distance for which the particle is swept downstream as $x/W \sim O(10^3)$ during the migration along the circular ring on the cross-section because the mean lateral force along the ring is roughly evaluated as 4×10^{-6} there, and the mean migration velocity is determined by the quasi-steady balance between the lateral lift and the Stokes drag.
- [21] T. Kajishima, S. Takiguchi, H. Hamasaki, and Y. Miyake, Turbulence structure of particle-laden flow in a vertical plane channel due to vortex shedding, *JSME J. B* **44**, 526 (2001).
- [22] N. Balci, B. Thomases, M. Renardy, and C. R. Doering, Symmetric factorization of the conformation tensor in viscoelastic fluid models, *J. Nonnewton. Fluid Mech.* **166**, 546 (2011).
- [23] N. Nakagawa, T. Yabu, R. Otomo, A. Kase, M. Makino, T. Itano, and M. Sugihara-Seki, Inertial migration of a spherical particle in laminar square channel flows from low to high Reynolds numbers, *J Fluid Mech.* **779**, 776 (2015).
- [24] Y. Matsuoka, Y. Nakayama, and T. Kajiwara, Effects of viscoelasticity on shear-thickening in dilute suspensions in a viscoelastic fluid, *Soft Matter* **16**, 728 (2020).